NJC

ROYAL SOCIETY OF CHEMISTRY

COMMUNICATION

View Article Online
View Journal | View Issue

Cite this: *New J. Chem.*, 2022, **46**, 4057

Received 14th December 2021,
Accepted 15th February 2022

DOI: 10.1039/d2nj00755j

rsc.li/njc

Crystalline azobenzene composites as photochemical phase-change materials†

Kieran Griffiths, *[a] Nathan R. Halcovitch [a] and John M. Griffin [ab]

Traditional phase change materials can store latent heat with high energy density providing they are stored above the phase transition temperature. In contrast, photochemical phase change materials allow latent heat storage at, or below, ambient temperatures and heat release can be triggered using heat or light stimuli. Herein, we report that crystalline binary mixtures of azobenzene and 4-methoxyazobenzene form photochemical phase change materials that possess working temperatures in the range of −58 °C to 31 °C. These mixtures can store and release up to 266 J g^{-1} of latent heat energy.

With the development of renewable energy technologies, the intermittent nature of wind and solar energy has meant that storage has become a key consideration. For thermal energy, phase-change materials (PCMs) are widely used to store waste heat for later use. However, PCMs need to be stored above the phase-transition temperature and so require efficient insulation to prevent radiative heat-loss. Recently, molecular photoswitches have been incorporated into PCMs to provide photochemical control over the mechanism and temperature of heat release.[1] Incorporation of photoswitches also allows renewable solar energy to be directly stored in the chemical bonds of the metastable photoisomer. An external stimulus, such as heat or photoirradiation, can drive reconversion to the ground state isomer which releases the stored energy as heat, and in PCMs, can also trigger a phase change. Azobenzene (AZB) has been extensively studied for this application due to its chemical stability, ease of synthesis and its metastable *Z* isomer which allows energy storage in the form of molecular strain energy (52.4 kJ mol^{-1}).[2–7] The *Z* isomer can be generated through photoisomerization in the presence of UV light, and the stored energy can be released as heat by subsequent $Z \rightarrow E$ reconversion either driven thermally or through exposure to >400 nm light.[7,8] Through various methods of functionalisation, amorphous AZB has been shown to switch in the solid state.[9,10] However, for the crystalline form the $E \rightarrow Z$ photoisomerization of AZB is suppressed due to the lack of conformational freedom in the crystalline phase.

Photoliquefiable AZB derivatives which can change from solid to liquid at room temperature, should receive considerable attention because of their inherent superiority in $E \rightarrow Z$ conversion without solvent assistance.[11,12] As well as storing energy in the metastable *Z* isomer, the solid → liquid phase change upon $E \rightarrow Z$ isomerisation stores additional energy which is recovered as an exothermic lattice enthalpy when the material recrystallises during $Z \rightarrow E$ reconversion. Indeed, both AZB and arylazo pyrazole materials have been tailored to benefit from this type of energy storage mechanism.[13–15] Furthermore, the photo-induced *Z* isomers help to decrease the melting point of the resultant *E*/*Z* mixture, which is the key to the photo-melting effect of many photoliquefiable derivatives at room temperature.

A key limitation of photoliquifiable AZB derivatives is the melting point of the *Z*-isomer-rich form, as the material needs to be in the liquid phase to allow $Z \rightarrow E$ reconversion and therefore energy release. This imposes a lower temperature limit for photoliquefiable PCMs to function. Therefore, reducing the melting point of the *Z*-isomer-rich phase is a key target in expanding the working temperature range.

A potential route to lowering the melting point of the AZB system is to form mixtures of AZB derivatives with different physical properties (Fig. 1). Considering a mixture of AZB derivatives **a** and **b**, in specific ratios it should be possible to form eutectic binary systems which are characterised by a lower melting temperature than either pure **a** or pure **b**. However, it is also important that the mixture of *E* isomers is solid at ambient temperature so a crystallisation enthalpy exotherm is visible on reconversion, in order to function as a PCM. When irradiated, the four-component mixture of *E*-**a**, *Z*-**a**, *E*-**b** and *Z*-**b** should

[a] *Department of Chemistry, Lancaster University, Lancaster LA1 4YB, UK. E-mail: k.griffiths1@lancaster.ac.uk*
[b] *Materials Science Institute, Lancaster University, Lancaster, LA1 4YB, UK*

† Electronic supplementary information (ESI) available. CCDC 2109112–2109123. For ESI and crystallographic data in CIF or other electronic format see DOI: 10.1039/d2nj00755j

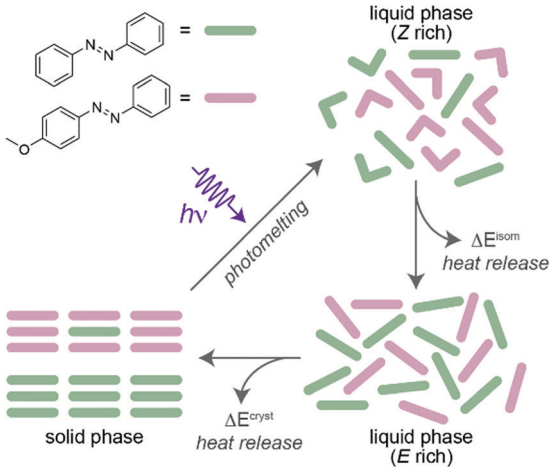

Fig. 1 Schematic demonstrating the energy storage principle in a eutectic/photomelting system [green = AZB (**1**) and pink 4-methoxyazobenzene (**2**)].

further reduce the melting point, enabling photomelting at temperatures below that of a single component.

In this work, azobenzene (**1**), Fig. 1, was chosen as the first energy storage element 4-methoxyazobenzene (**2**), Fig. 1, was chosen as the second energy storage element due to the low melting point of both *E* and *Z* isomers, which are 53 °C and 25 °C, respectively.[16,17] Hitherto, the melting point of the two-component mixture can be lower than either the *E* or *Z* isomers of **1** or **2**. Binary composites were synthesised by melting *E*-**1** and *E*-**2** in specific molar ratios together at 120 °C (Table 1, Fig. S1, ESI†). They were cooled to room temperature and the thermal cycle was repeated ten times to maximise sample homogeneity. On the final cooling cycle, the binary composites were cooled at 1 °C min^{-1} and crystalline solids formed. These binary mixtures, *E*-$\mathbf{1}_x$*E*-$\mathbf{2}_{(1-x)}$, were characterised by X-ray powder diffraction (XRPD) and single-crystal XRD (SC-XRD) (Table S1 and Fig. S2–S6, ESI†).

The XRPD pattern for *E*-**1** is consistent with the orthorhombic $P2_1/c$ space group which has been previously reported.[18] However, the pattern for *E*-**2** is biphasic and profile fitting (Fig. S3, ESI†) shows a dominant orthorhombic phase within the *Pmmm* space group and a minor orthorhombic $Pna2_1$ phase. The bi-phasic powder pattern remained consistent after multiple melting/crystallisation cycles. Single crystals of the minor phase of *E*-**2** were obtained by slow evaporation of a concentrated methanol solution. The structure reveals a herringbone arrangement with face-to-edge orientation of the molecules, as shown in Fig. S4 (ESI†). The lattice parameters are highly temperature dependent (Table S1, ESI†), with measurements between 100 to 290 K showing thermal expansion along the *c*-axis with an expansion coefficient of 130(5) M K^{-1} which is considered 'colossal' expansion. Large thermal expansion of azo-containing crystals has been reported previously and has been attributed to dynamic pedal-motion of the azo-group.[19,20]

From the composites, it was only possible to obtain a single-crystal for *E*-$\mathbf{1}_{0.1}$*E*-$\mathbf{2}_{0.9}$. The structure is consistent with the orthorhombic $Pna2_1$ space group observed for the minor phase of pure *E*-**2**. However, a key difference is that the *c*-axis for *E*-$\mathbf{1}_{0.1}$*E*-$\mathbf{2}_{0.9}$ is 1.5% shorter. The composite also displays a larger volumetric thermal expansion than pure *E*-**2** (Table S2, ESI†), which arises from an increased expansion along the *c*-axis, but this is somewhat offset by reduced expansion along the *b*-axis. XRPD of a bulk sample of *E*-$\mathbf{1}_{0.1}$*E*-$\mathbf{2}_{0.9}$ also shows a single phase in the same $Pna2_1$ space group (Fig. S5, ESI†). Interestingly, the inclusion of a small amount of **1** into the structure of **2** seems to exclusively produce a structure consistent with the minor phase of pure **2**. However, profile fitting of XRPD patterns for bulk *E*-$\mathbf{1}_x$*E*-$\mathbf{2}_{(1-x)}$ samples with higher contents of *E*-**1** (Table S3 and Fig. S6a–c, ESI†) show two phases which conform to the $Pna2_1$ space group observed for *E*-**2** and *E*-$\mathbf{1}_{0.1}$*E*-$\mathbf{2}_{0.9}$, and the $P2_1/c$ space group reported for *E*-**1**. ^{13}C CPMAS NMR spectra (Tables S4–S6 and Fig. S7, S8, ESI†) are consistent with the findings from XPRD. In particular, for *E*-$\mathbf{1}_x$*E*-$\mathbf{2}_{(1-x)}$ samples, the resonances show a pronounced broadening which is characteristic of increased disorder in the materials. There is a significant shifting of the characteristic resonances of *E*-**2** which are consistent with *E*-**1** molecules substituting into the $Pna2_1$ structure. Overall, the structural characterisation shows that the composite structures adopt two phases based on either the *E*-**1** structure or the minor phase of *E*-**2**. For low proportions of *E*-**1**, there is only a single phase, which is the minor phase of *E*-**2**. To investigate the thermal properties of *E*-**1**, *E*-**2** and the binary composites *E*-$\mathbf{1}_x$*E*-$\mathbf{2}_{(1-x)}$, cyclic DSC measurements were performed (Fig. 2 and Table S7, ESI†). Cycles were repeated five times and the thermal features were identical on each run. Thermograms of pure *E*-**1** and *E*-**2** show transitions for melting and crystallisation on the heating and cooling branches, respectively. The observed melting points of the pure compounds are in good agreement with literature values.[16]

For the binary composites, multiple endothermic features are observed on the heating branch. For all three mixtures the onset of the lowest melting transition (solidus) is between 31.2 and 34.2 °C which is attributed to the melting of the

Table 1 Compositional and Thermal data for $\mathbf{1}_x\mathbf{2}_{(1-x)}$ binary composites

Sample	Mole fraction of *E*-**1**/*E*-**2**	Melting onset *E*-form/°C	Δ*H* (cryst. *E*–form)/ kJ mol^{-1}	Δ*H* (isom. *Z*–*E*)/ kJ mol^{-1}	Δ*H* (total)/ KJ mol^{-1}	Δ*H* (total)/J g^{-1}	PSS *Z*-**1**/*Z*-**2** (%)	Half-life *Z*-**1**/*Z*-**2**/hours	Melting onset *E*/*Z*-**1**,**2**/°C
E-**1**	1.00/0.00	53.0	24.16	0	24.16	132.6	0/—	—	n/a
E-$\mathbf{1}_{0.75}$*E*-$\mathbf{2}_{0.25}$	0.25/0.75	33.1	19.47	24.25	43.72	230.4	19/89	27.4/50.2	−55.1
E-$\mathbf{1}_{0.5}$ *E*-$\mathbf{2}_{0.5}$	0.50/0.50	31.2	15.42	33.25	48.67	246.8	22/77	22.7/53.3	−58.2
E-$\mathbf{1}_{0.25}$*E*-$\mathbf{2}_{0.75}$	0.75/0.25	34.2	15.64	38.82	54.46	266.0	25/71	24.7/58.7	−53.1
E-**2**	0.00/1.00	53.8	20.91	45.97	66.88	315.1	—/68	-/55.5	−25.5

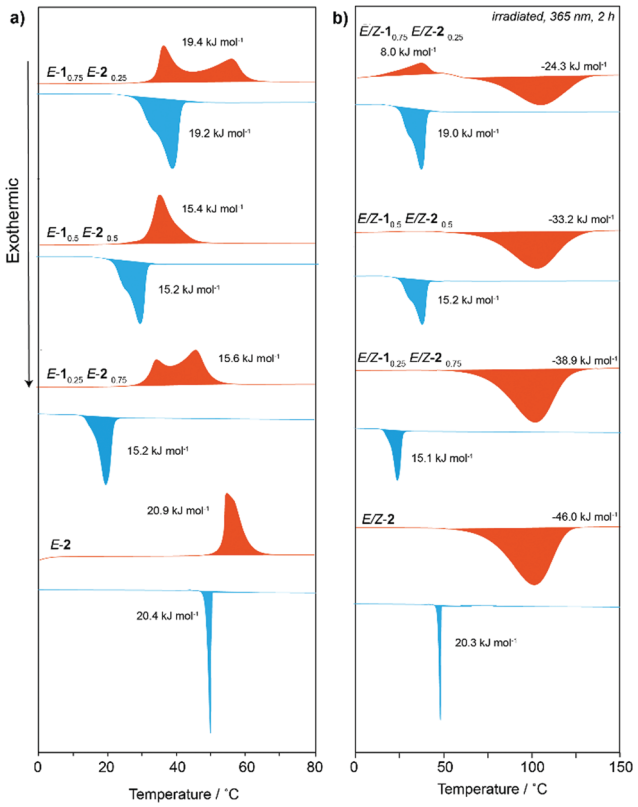

Fig. 2 DSC first heating branches (red) and first cooling branches (blue) of (a) E-$\mathbf{1}_x E$-$\mathbf{2}_{(1-x)}$, and (b) irradiated E/Z-$\mathbf{1}_x E/Z$-$\mathbf{2}_{(1-x)}$ composites. Thermograms were obtained at a heating rate of 2.5 °C min^{-1}.

eutectic mixture and is confirmed by microscopy (Fig. S9, ESI†). For E-$\mathbf{1}_{0.75}E$-$\mathbf{2}_{0.25}$ and E-$\mathbf{1}_{0.25}E$-$\mathbf{2}_{0.75}$, two distinct endotherm peaks are observed. The first corresponds to melting of the eutectic composition at lower temperatures 35.5 °C and 34.4 °C, respectively, and a second melting transition (liquidus) at higher temperatures 56.5 °C and 47.2 °C respectively, which corresponds to the melting of the major component, either E-**1** for E-$\mathbf{1}_{0.75}E$-$\mathbf{2}_{0.25}$ or E-**2** for E-$\mathbf{1}_{0.25}E$-$\mathbf{2}_{0.75}$. The thermogram for E-$\mathbf{1}_{0.5}E$-$\mathbf{2}_{0.5}$ only shows a eutectic melting transition and therefore must consist of the homogenously mixed liquid phase which is close to the eutectic composition. The DSC data shows that each composition contains a proportion of the eutectic mixture which melts at the eutectic melting point and drives the dissolution/melting of the remaining composite. Due to the overlap between the solidus and liquidus in E-$\mathbf{1}_{0.75}E$-$\mathbf{2}_{0.25}$ and E-$\mathbf{1}_{0.25}E$-$\mathbf{2}_{0.75}$ it is difficult to precisely determine the enthalpy associated with each transition. However, the overall endothermic energy density of each binary mixture is lower than the pure crystalline component. For example, E-$\mathbf{1}_{0.5}E$-$\mathbf{2}_{0.5}$ has a single eutectic melting transition with an enthalpy of 15.4 kJ mol^{-1}, which is noticeably lower than E-**1** (24.2 kJ mol^{-1}) and E-**2** (20.9 kJ mol^{-1}).

The binary composites, E-$\mathbf{1}_x E$-$\mathbf{2}_{(1-x)}$, were irradiated with 365 nm light at room temperature. As expected, E-**1** does not photo-melt whereas E-**2** photomelts to form a viscous red liquid (Fig. S10, ESI†). All composites were observed to photo-melt, which indicates the melting point of the E/Z mixtures is below room temperature (Fig. S10, ESI†).[17]

The E:Z ratio of both **1** and **2** in the composites was monitored by ^{1}H NMR spectroscopy to determine the photostationary state (PSS) (Table 1, Fig. S11 and Table S8, ESI†). Interestingly, the binary composites (Table 1, entries 2–4) allow the photoisomerisation of **1** from the E to Z state, which is prevented in pure crystalline **1** due to the dense molecular packing (Table 1, entry 1). Whether this is due to solubilisation in photo-melted E/Z-**2** or as a consequence of the incorporation of E-**1** within the $Pna2_1$ phase of E-**2** is unclear. However, for both **1** and **2** in the composites, the mole fraction of each component directly affects the PSS. Table 1 shows that the E/Z content at the PSS for both **1** and **2** decreases with increasing mole fraction. For **2**, where the Z isomer content at the PSS is consistent with the photo-melted literature value (68%),[7] even a small quantity of **1** increases the population of Z-**2**, reaching a maximum of 89% for E-$\mathbf{1}_{0.75}E$-$\mathbf{2}_{0.25}$ (Table 1, entry 2).

A similar trend is observed for **1** when the proportion of **2** is increased, albeit with a considerably lower maximum Z-**1** content of 25% (Table 1, entry 4). Even when fully photo-melted, none of the samples reach a PSS of 100% Z isomer, despite the fact that this is achievable for pure **2** when solubilised in benzene (Fig. S12, ESI†). Repetitions of the irradiation procedure for E-**2** with varying sample thickness gave the same PSS, suggesting the maximum proportion of Z-**2** is not limited by light penetration.

To investigate the effect of UV irradiation on the thermal properties, DSC measurements were performed on the binary composites after 2 hours of irradiation at 365 nm (Fig. 2, full data Table S9a, b, ESI†). For each composite, on the heating branch the eutectic and major component melting transitions are significantly reduced or eliminated because they form a pseudo-four-component melt which is indicative of mixed E/Z AZB systems.[17] In contrast to the unirradiated samples, an exotherm is observed corresponding to thermally-driven $Z \rightarrow E$ reconversion. These features onset between 73–76 °C and the exotherm magnitude increases with the mole fraction of **2**, which is consistent with the considerably higher PSS and experimental energy difference between E and Z forms for **2** (69.2 kJ mol^{-1}, see Table S10, ESI†) compared to **1** (52.4 kJ mol^{-1}).[21] On the cooling branches, for each sample an endotherm is observed which is consistent with the crystallisation of the E-$\mathbf{1}_x E$-$\mathbf{2}_{(1-x)}$ mixtures in their unirradiated forms. For irradiated E/Z-$\mathbf{1}_{0.75}E/Z$-$\mathbf{2}_{0.25}$ a small broad endothermic transition is observed at 34.1 °C on the first heating branch which is attributed to a residual amount of solid E-$\mathbf{1}_{0.75}E$-$\mathbf{2}_{0.25}$.

The expected magnitudes of the $Z \rightarrow E$ exotherms were calculated for each of the E/Z-$\mathbf{1}_x E/Z$-$\mathbf{2}_{(1-x)}$ composites. These values are based on the experimental E–Z energy differences for **1** and **2** above, the experimental PSS after 2 h of irradiation and the mass fraction of **1** and **2** in each mixture (Tables S11 and S12, ESI†). The calculated exotherm magnitudes show good agreement with the experimental values (Fig. S13, ESI†) which indicates the enthalpy is not significantly affected by intermolecular interactions in the liquid mixtures. At the end of the

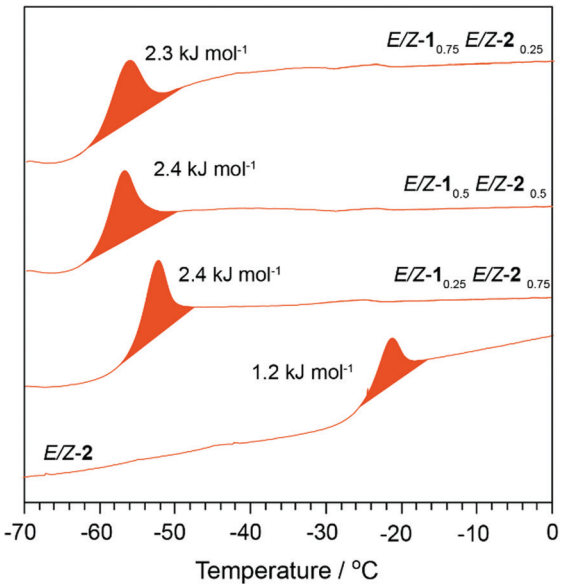

Fig. 3 DSC first heating branches (red) of irradiated *E/Z*-$\mathbf{1}_x$*E/Z*-$\mathbf{2}_{(1-x)}$ composites. Thermograms were obtained at a heating rate of 2.5 °C min^{-1} between −70 to 0 °C.

heating branch, the *Z*-**1**/**2** molecules have thermally relaxed to *E*-**1**/**2**. The materials now have the structural properties of non-irradiated *E*-$\mathbf{1}_x$*E*-$\mathbf{2}_{(1-x)}$, and therefore the exothermic crystallisation transition is observed on the cooling branch (Fig. 2 and Table S9, ESI†). This means that over one full heating and cooling cycle there are net energy outputs of 130.4 J g^{-1} (*E/Z*-$\mathbf{1}_{0.75}$*E/Z*-$\mathbf{2}_{0.25}$); 246.8 J g^{-1} (*E/Z*-$\mathbf{1}_{0.5}$*E/Z*-$\mathbf{2}_{0.5}$); 266.0 J g^{-1} (*E/Z*-$\mathbf{1}_{0.25}$*E/Z*-$\mathbf{2}_{0.75}$) and 315.1 J g^{-1} (*E/Z*-**2**).

Although the gravimetric energy density of the composites is deceased when compared to *E*-**2**, another important property is the temperature range within which the materials can be photomelted. In this system, this is dependent on the melting point of the irradiated *E/Z* composites. To determine these, DSC cycles between −70 and 0 °C were performed on photomelted *E/Z*-$\mathbf{1}_x$*E/Z*-$\mathbf{2}_{(1-x)}$ composites Full thermal data and the first heating branch is shown in Fig. 3 and Table S13 (ESI†). Photomelted *E/Z*-**2** shows an endothermic feature at −25.6 °C with an enthalpy of −1.2 kJ mol^{-1}. This feature is consistent with a solidification and/or glass transition and represents the temperature at which the mobility of the molecules is significantly reduced (Fig. S14, ESI†). The *E/Z*-$\mathbf{1}_x$*E/Z*-$\mathbf{2}_{(1-x)}$ composites show similar transitions but the onset temperature decreases considerably for each sample. The lowest onset is for *E/Z*-$\mathbf{1}_{0.5}$*E/Z*-$\mathbf{2}_{0.5}$ at −58.2 °C and all samples show a decrease of more than 25 °C compared to *Z*-**2**. The energy release of the irradiated composites here is demonstrated in the DSC measurements by thermal reconversion to the ground-state *E* isomer, but above the transition temperature, it could also be released through photoconversion to the *E* isomer by irradiating with >400 nm light.[22] The significantly wider mobile range of the composites than pure *E/Z*-**2** significantly increases the temperature range over which the energy can be released by light irradiation.

The thermal reconversion kinetics of *Z* isomers in the *E/Z*-$\mathbf{1}_x$*E/Z*-$\mathbf{2}_{(1-x)}$ composites show first-order Arrhenius behaviour which is expected for these systems (Table S14a–e and Fig. S15a–d, ESI†). Linear fits give *Z*-**1** and *Z*-**2** half-lives between 22–27 hours and 50–59 hours respectively. The half-life of *Z*-**1** in solution at ambient temperature is on the order of 100 hours,[23] whereas the half-life of *Z*-**2** in benzene solution is 38.5 hours (Table S15a, b and Fig. S16, ESI†). Considering that *Z*-**2** comprises much of the energy storage of these materials, this is a moderate increase.

The thermally-induced reversible phase transition gives the $\mathbf{1}_x\mathbf{2}_{(1-x)}$ composites the properties of a photochemical PCM where thermal energy can be stored above the solid → liquid phase transition, and recovered through reversal of the phase transition upon cooling. Formation of a eutectic phase considerably improves the working temperature range of the PCM without significantly affecting the energy density of the material. It should be possible to increase the energy density further by making chemical alterations to increase the intrinsic energy difference between isomers, and also to increase the maximum PSS of each component.

Author contributions

The manuscript was written through contributions of all authors. All authors have given approval to the final version of the manuscript.

Conflicts of interest

There are no conflicts to declare.

Acknowledgements

We are grateful to the Leverhulme Trust for funding this project (Research Project Grant Number RPG-2018-395).

Notes and references

1 Y. Shi, M. A. Gerkman, Q. Qiu, S. Zhang and G. G. D. Han, *J. Mater. Chem. A*, 2021, **9**, 9798–9808.
2 G. D. Han, S. S. Park, Y. Liu, D. Zhitomirsky, E. Cho, M. Dincă and J. C. Grossman, *J. Mater. Chem. A*, 2016, **4**, 16157–16165.
3 E. Durgun and J. C. Grossman, *J. Phys. Chem. Lett.*, 2013, **4**, 854–860.
4 T. J. Kucharski, N. Ferralis, A. M. Kolpak, J. O. Zheng, D. G. Nocera and J. C. Grossman, *Nat. Chem.*, 2014, **6**, 441–447.
5 A. R. Dias, M. E. Minas Da Piedade, J. A. Martinho Simões, J. A. Simoni, C. Teixeira, H. P. Diogo, Y. Meng-Yan and G. Pilcher, *J. Chem. Thermodyn.*, 1992, **24**, 439–447.
6 H. K. Cammenga, V. N. Emel'yanenko and S. P. Verevkin, *Ind. Eng. Chem. Res.*, 2009, **48**, 10120–10128.
7 K. Masutani, M. A. Morikawa and N. Kimizuka, *Chem. Commun.*, 2014, **50**, 15803–15806.

8 L. Dong, Y. Feng, L. Wang and W. Feng, *Chem. Soc. Rev.*, 2018, **47**, 7339–7368.
9 D. Zhitomirsky, E. Cho and J. C. Grossman, *Adv. Energy Mater.*, 2016, **6**, 1502006.
10 M. Baroncini, S. D'Agostino, G. Bergamini, P. Ceroni, A. Comotti, P. Sozzani, I. Bassanetti, F. Grepioni, T. M. Hernandez, S. Silvi, M. Venturi and A. Credi, *Nat. Chem.*, 2015, **7**, 634–640.
11 K. Ishiba, M. Morikawa, C. Chikara, T. Yamada, K. Iwase, M. Kawakita and N. Kimizuka, *Angew. Chem., Int. Ed.*, 2015, **54**, 1532–1536.
12 Y. Norikane, E. Uchida, S. Tanaka, K. Fujiwara, E. Koyama, R. Azumi, H. Akiyama, H. Kihara and M. Yoshida, *Org. Lett.*, 2014, **16**, 5012–5015.
13 M. A. Gerkman, R. S. L. Gibson, J. Calbo, Y. Shi, M. J. Fuchter and G. G. D. Han, *J. Am. Chem. Soc.*, 2020, **142**, 8688–8695.
14 Z.-Y. Zhang, Y. He, Z. Wang, J. Xu, M. Xie, P. Tao, D. Ji, K. Moth-Poulsen and T. Li, *J. Am. Chem. Soc.*, 2020, **142**, 12256–12264.
15 Q. Qiu, Y. Shi and G. G. D. Han, *J. Mater. Chem. C*, 2021, **9**, 11444–11463.
16 Y. Norikane, S. Tanaka and E. Uchida, *CrystEngComm*, 2016, **18**, 7225–7228.
17 S. Eligehausen, S. M. Sarge, G. Öhlschläger and H. K. Cammenga, *J. Therm. Anal.*, 1989, **35**, 515–526.
18 J. A. Bouwstra, A. Schouten and J. Kroon, *Acta Crystallogr., Sect. C*, 1983, **39**, 1121–1123.
19 N. Juneja, D. K. Unruh, E. Bosch, R. H. Groeneman and K. M. Hutchins, *New J. Chem.*, 2019, **43**, 18433–18436.
20 K. M. Hutchins, D. K. Unruh, F. A. Verdu and R. H. Groeneman, *Cryst. Growth Des.*, 2018, **18**, 566–570.
21 J. Hu, S. Huang, M. Yu and H. Yu, *Adv. Energy Mater.*, 2019, **9**, 1901363.
22 J. Henzl, M. Mehlhorn, H. Gawronski, K.-H. Rieder and K. Morgenstern, *Angew. Chem., Int. Ed.*, 2006, **45**, 603–606.
23 J. Olmsted, J. Lawrence and G. G. Yee, *Sol. Energy*, 1983, **30**, 271–274.